Microporous and Mesoporous Materials 158 (2012) 324–331

Contents lists available at SciVerse ScienceDirect

Microporous and Mesoporous Materials

journal homepage: www.elsevier.com/locate/micromeso

Naphthalene-based periodic nanoporous organosilicas: I. Synthesis and structural characterization

Konstantinos Dimos [a,b,*], Myrsini K. Antoniou [c], Aimilia Meichanetzoglou [a], Smaragda Lymperopoulou [a], Maria-Dimitra Ouzouni [a], Ioannis B. Koutselas [b], Demosthenes Fokas [a], Michael A. Karakassides [a], Raffaele G. Agostino [c], Dimitrios Gournis [a]

[a] Department of Materials Science and Engineering, University of Ioannina, GR-45110 Ioannina, Greece
[b] Department of Materials Science, University of Patras, GR-26504 Patras, Greece
[c] CNISM-Department of Physics, University of Calabria, via P. Bucci 33C, IT-87036 Rende (Cosenza), Italy

ARTICLE INFO

Article history:
Received 14 January 2012
Received in revised form 13 March 2012
Accepted 14 March 2012
Available online 28 March 2012

Keywords:
Naphthalene
Grafting
Periodic mesoporous organosilicas
Nanoporous
Luminescence

ABSTRACT

Novel periodic nanoporous organosilicas (PNOs) were synthesized by direct co-condensation of tetraethylorthosilicate and of the prior synthesized compound triethoxy(naphthalen-1-yl)silane. Structural characterization of materials was performed with various techniques such as ^{1}H and ^{13}C nuclear magnetic resonance, X-ray powder diffraction, Fourier transform infrared spectroscopy, ultraviolet–visible and photoluminescence emission and excitation spectroscopy, differential thermal and thermo-gravimetric analyses, nitrogen porosimetry and helium pycnometry. Naphthalene-based moieties were grafted on the silicate matrix through oxygen bonds resulted to novel organosilicate final materials that exhibited high naphthalene content up to 17 wt.% with a corresponding 1.33 mmol/g molar concentration, high crystallinity, specific surface area larger than 1000 m^2/g and pore size distributions in the microporous/mesoporous boundary. Optical properties have been found to be comparable to the naphthalene. The attachment of the optically active part to the mesopores walls and its specific tuning for blue/UV luminescence demonstrates that this type of the reported low cost materials can be considered as phosphors in UV Leds. Tuning by using the red shift of similar larger molecules, all simultaneously trapped within the PNO, may prove to be efficient white light phosphor. Moreover, the nonlinear active properties of the active naphthalene may also allow for novel applications. Finally, materials were studied for hydrogen and methane storage with Sieverts' apparatus and demonstrated high H_2 and CH_4 weight proportions for PNOs materials at various temperatures up to 4.3 MPa and 3.5 MPa respectively as presented in part II.

1. Introduction

Synthesis of ordered mesoporous solids based either on silica or pure carbon is considered as breakthrough in numerous scientific fields and applications. Since the first report of mesoporous M41S materials produced by Mobil in 1992 [1,2], many similar solids have been synthesized like SBA, MSU, FDU, KIT and CMK [3–10]. The high surface areas, combined with narrow and tunable pore size distributions of this kind of materials allow them to serve as ideal absorbents, catalysts, sensors, etc. A further major breakthrough in this field was the development of periodic mesoporous (or nanoporous) organosilicas (PMOs or PNOs) in which organic groups are located within the channel walls as bridges between Si centres [11–13]. Although according to the strict definition of PNOs that these materials are obtained only by the use of bissilylated organic precursors [14], their classification may be generalized to include solids derived from analogous monosilylated organic precursors since the final hybrid organic–inorganic products exhibit same properties. These materials are produced by direct synthesis with co-condensation of appropriate organosilicate precursors with TEOS or TMOS [15], while, with post-synthetic method by grafting organic moieties on the silicate matrix through oxygen bonds, comparable functionalized ordered mesoporous materials are obtained [16]. As reported in the recent literature, various organic groups have been used for both synthetic procedures like diurea [17,18], glycine-based [19], thiol groups [20,21] and more frequently groups containing aromatic rings [22,23].

PNOs exhibit basic properties owned in their ordered mesoporous structure as high specific surface areas, narrow pore size distribution and high crystallinity, while depending on the precursor their properties can be tuned or be targeted on specific applications. While the co-condensation technique demonstrates significant advantages as homogeneity and stability, materials

* Corresponding author at: Department of Materials Science and Engineering, University of Ioannina, GR-45110 Ioannina, Greece. Tel.: +30 26510 07367; fax: +30 26510 07074.
E-mail address: kdimos@cc.uoi.gr (K. Dimos).

1387-1811/$ - see front matter © 2012 Elsevier Inc. All rights reserved.
http://dx.doi.org/10.1016/j.micromeso.2012.03.037

produced with this method share one main disadvantage, *i.e.* the limitations in the organic content molecule selection rising by the lack of crystallinity when high organosilicate precursor ratios are used. PNOs have been recently used as fillers for liquid chromatography separation [24], as catalysts [25,26], as sensors for electrochemical detection [27], as drug delivery carriers [17,18], as matrices for enzyme immobilization [19], as heavy metal absorbents [28] and many other applications as reported in recent review articles [22,23,29].

Furthermore, in the last two years as leaded by the group of Inagaki et al. [30–34], PNOs or functionalized mesoporous silicas with optical properties like photoluminescence have been reported, based mainly on phenyl rings [30–36], while PNOs have been also used for hydrogen and methane storage [37,38]. In the latest related application it has been found that the presence of aromatic rings leads to higher adsorption rates compared to other systems [39]. Crucial characteristics of PNOs as high specific surface areas, low density and the fact that they are tailored-made materials concerning both pore diameter and the contained functional groups places them as ideal materials for gas physisorption and storage. In this sense, in the present work is reported the synthesis and fully characterization of naphthalene containing PNOs to be tested for hydrogen and methane storage as presented in part II [40], as well as for other optical applications. These samples are derived from a monosilylated organic precursor, triethoxy(naphthalen-1-yl)silane, in contrary with the few reports in literature for naphthalene containing PNOs which were all obtained by the bissilylated 2,6-bis(triethoxysilyl)naphthalene used recently by Inagaki's group [30,31]. It is believed that by using monosilylated organic precursor the effect of the tail parts of the modified naphthalene molecule on the optically active states will be less pronounced, allowing for further tuning of the final materials.

2. Experimental

2.1. Reagents

All materials were of reagent or analytical grade and were used as purchased without further purification. Magnesium powder 99% was purchased from Fluka, tetraethylorthosilicate (TEOS) 98% from Sigma–Aldrich, anhydrous THF over molecular sieve 99.5% from Sigma–Aldrich, 1,2-dibromoethane 99% from Alfa, 1-bromonaphthalene 97% from Alfa, hexane 95% from Merck, ethyl acetate 99.5% from Merck, ammonium chloride (NH_4Cl) 99% from Merck, sodium sulphate (Na_2SO_4) 99% from Panreac, aqueous ammonia solution (NH_3) 25 wt.% from Fluka, cetyltrimethylammonium bromide (CTAB) 95% from Sigma–Aldrich, ethanol (EtOH) 99.5% from Panreac and hydrochloric acid (HCl) 37 wt.% from Merck.

2.2. Synthesis of triethoxy(naphthalen-1-yl)silane

Triethoxy(naphthalen-1-yl)silane (hereafter: Naph-Si) was prepared from 1-bromonaphthalene and TEOS via a modified protocol of a sonochemical Barbier-type reaction [41] according the following reaction:

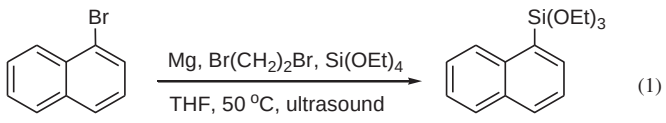

(1)

Synthesis of Naph-Si was performed as follows: a mixture of 1.4 g (57.6 mmol) of Mg powder, 21.4 mL (95.9 mmol) of TEOS and 5 mL of anhydrous THF, heated at 50 °C in an ultrasonic bath sonicator, was treated dropwise first with 1.1 mL (12.8 mmol) of 1,2-dibromoethane and then with 2.7 mL (19.4 mmol) of 1-bromonaphthalene. The magnesium powder was immediately dissolved and a dark green coloured solution was observed. The reaction mixture was heated at 50 °C for 1 h, cooled at room temperature and then treated with 30 mL of hexane. The resulting white precipitate was filtered and the filtrate was washed with 5% aq. NH_4Cl. The organic phase was dried over Na_2SO_4, filtered and concentrated under vacuum to give the crude product. Purification by flash chromatography on silica gel with ethyl acetate–hexane (5:95) as an eluent, afforded 1.12 g (20%) of triethoxy(naphthalen-1-yl)silane as a pale yellow oil.

Nuclear magnetic resonance (NMR) spectroscopy was used to certify the successful synthesis of Naph-Si. ^1H and ^{13}C NMR spectra of the synthesized Naph-Si, were recorded at 25 °C on a 500 MHz Bruker Avance DRX NMR spectrometer operating at 500 and 125.7 MHz respectively, running on TopSpin 1.2 (Bruker Biospin Ltd.) and using deuterated chloroform ($CDCl_3$) as solvent. ^1H NMR spectra were acquired in the Fourier transform (FT) mode with 32 K data points, 16 free induction decays (FID), relaxation delay of 5 s and spectral widths of 5252 Hz. All FIDs were multiplied by an exponential weighting function corresponding to a 0.3 Hz line-broadening factor prior to Fourier transformation. ^{13}C NMR spectra were recorded with 64 K data points, 512 free induction decays (FID), relaxation delay of 2 s and spectral widths of 29762 Hz. A 1 Hz line-broadening factor prior to Fourier transformation was used. The acquired NMR spectra were manually corrected for phase and baseline distortions with TopSpin 1.2 (Bruker Biospin Ltd.) and referenced to the tetramethylsilane (TMS) peaks (δ ^1H 0.0, δ ^{13}C 0.0).

^1H and ^{13}C NMR spectra, available as Supplementary data, resulted the following: 500 MHz ^1H NMR ($CDCl_3$) δ 8.30 (d, 1 H, J = 8.3 Hz), 7.95 (dd, 1 H, J = 1.2, 7.9 Hz), 7.86 (d, 1 H, J = 8.2 Hz), 7.78 (d, 1 H, J = 7.8 Hz), 7.49–7.38 (m, 3 H), 3.83 (q, 6 H, J = 7.1 Hz), 1.18 (t, 9 H, J = 7.0 Hz). 125.7 MHz ^{13}C NMR ($CDCl_3$) δ 137.05, 136.22, 133.25, 131.11, 129.00, 128.63, 128.58, 126.25, 125.59, 124.98, 58.75, 18.23. ^1H and ^{13}C NMR data come in full agreement with those reported in literature [42].

2.3. Synthesis of periodic nanoporous organosilicas

Periodic nanoporous organosilica was synthesized with a one step direct co-condensation of TEOS and Naph-Si in a 6.33:1 molar ratio. 12.525 g H_2O, 8.058 g NH_3 (25 wt.%) and 0.315 g CTAB were stirred for 15 min in a 30 mL polypropylene bottle. 1.425 g TEOS (6.84 mmol) and 0.3138 g Naph-Si (1.08 mmol) were added and the solution was vigorously stirred for another 30 min. The beige product was retrieved after heat treatment at 80 °C for 96 h, which can be slightly considered as a hydrothermal treatment. It was filtered, rinsed with H_2O and cold ethanol and finally placed on a plate for air-drying (sample: Naph-PNO). 600 mg Naph-PNO were treated with 4.5 g HCl (37 wt.%) in 100 mL EtOH for 1 h at 70 °C. The product was then filtered, rinsed with cold EtOH and afterwards was placed on a plate for air-drying (sample: Naph-PNO-H^+). 240 mg Naph-PNO were placed in a porcelain crucible and were heat treated at 350 °C for 5 h with a 1.5 °C/min heating rate (sample: Naph-PNO-350).

2.4. Characterization

X-ray powder diffraction data were collected on a D8 Advance Bruker diffractometer using Cu K_α (40 kV, 40 mA, λ = 1.54178 Å) radiation and a secondary beam graphite monochromator. Diffraction patterns were collected in the 2θ range from 2° to 80°, in steps of 0.02° and 2 s counting time/step.

Infrared spectra were measured on a Perkin Elmer GX, Fourier transform spectrometer in the frequency range of 400–4000 cm^{-1}. Samples were dispersed pulverized in the form of KBr pellets were used for recording the spectra, which were the average of 64 scans at 2 cm^{-1} resolution.

UV–vis spectra were recorded on a Shimadzu UV-2401PC two beam spectrophotometer in the range of 200–800 nm, at a step of 0.5 nm, using combination of deuterium and halogen lamps as sources. Spectra were obtained from thin deposits obtained from mechanical grinding on quartz plates. These have also been confirmed to be the same as those obtained from diffuse reflectance experiments of solid pressed pellets, through the Kubelka–Monk relation.

The photoluminescence (PL) and photoluminescence excitation (PLE) spectra were obtained from solid pressed pellets or thick deposits on quartz plates, mounted in a Hitachi F-2500 FL spectrophotometer employing a xenon 150 W lamp and a R928 photomultiplier. The excitation and detection slits were set at 2.5 nm spectral bandwidth. All optical UV–vis and PL/PLE spectra were recorded at room temperature.

Thermo-gravimetric analysis (TG) and differential thermal analysis (DTA) were performed using a Perkin Elmer Pyris Diamond TG/DTA instrument. Samples of approximately 5 mg were heated in air from 25 °C to 900 °C, with a 5 °C/min rate.

The nitrogen adsorption–desorption isotherms were measured at −196 °C on a Sorptomatic 1990, thermo Finnigan porosimeter. Specific surface areas (S_{BET}) were determined with the Brunauer–Emmett–Teller (BET) method using adsorption data points in the relative pressure P/P_0 range 0.01–0.30. Surface areas (S_t) were also determined from t-plots which were constructed using nitrogen adsorption data on a nonporous-hydroxylated silica standard. The Kelvin equation was used according to the Barrett–Joyner–Halenda (BJH) method for calculation of core radii and the pore size distribution (PSD) of the samples, while for comparison reasons calculations were also performed using the Lennard-Jones potential functions according to the Horvath–Kawazoe (H–K) method and the Kruk–Jaroniec–Sayari (KJS) geometrical model. All samples used for the surface analyses were outgassed at 150 °C for 16 h under high vacuum (10^{-5} mbar) before the measurements. Skeletal densities of the samples have been measured with helium pycnometry at room temperature and atmospheric pressure using an appropriate novel apparatus (f-PcT – DeltaE S.r.l) replacing and optimizing different parts of similar apparatus described in Ref. [43].

3. Results and discussion

X-ray powder diffraction (XRD) patterns in the low angle region of the samples Naph-PNO, Naph-PNO-H^+ and Naph-PNO-350 are shown in Fig. 1. All three patterns are typical of materials with hexagonal arrangement of uniform pores displaying the characteristic strong reflection at low scattering angles 2θ as well as the next two reflection peaks (1 1 0) and (2 0 0) [1,2]. All three samples are classified in the *P6mm* space group, thus, the first reflection peak is attributed to Miller (1 0 0) lattice planes. Specifically, the XRD pattern of sample Naph-PNO (1a) displays three reflection peaks corresponding to the d_{100}, d_{110} and d_{200} planed spacing. Applying Bragg's law for the first reflection peak yields d_{100} spacing of 41.6 Å. Pattern (1b) of sample Naph-PNO-H^+ shows also the first three reflection peaks with a d_{100} spacing of 42.4 Å, while d_{100} spacing of sample Naph-PNO-350 in pattern (1c) is 38.1 Å. These suggest that there is an expected small shrinkage of the matrix silicate network due to the heat treatment in spite of maintaining the wide range hexagonal pore ordering [44]. The observed shrinkage is undoubtedly attributed to the formation of more oxygen bridges that bind the matrix. More information about the pore structure

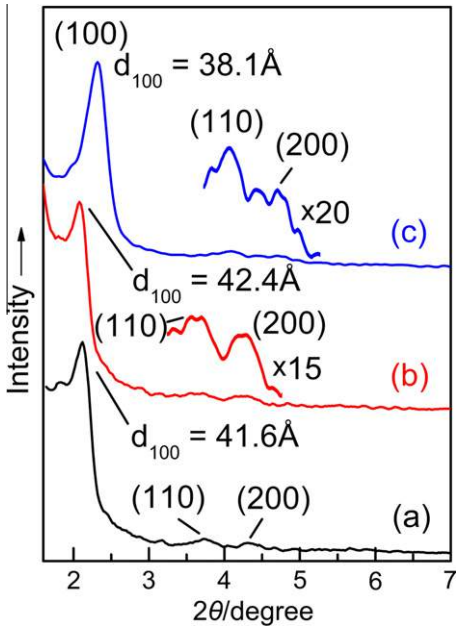

Fig. 1. X-ray powder diffraction patterns in the low angle region for samples Naph-NO (a), Naph-PNO-H^+ (b) and Naph-PNO-350 (c).

and the exact matrix wall width of all samples arises from nitrogen adsorption–desorption measurements (see below).

Fig. 2 shows the Fourier transform infrared spectra of samples Naph-PNO, Naph-PNO-H^+ and Naph-PNO-350. Spectrum (2a) of pristine Naph-PNO exhibits absorption peaks at ν_{max}: 465, 800, 960, 1080 and 1223 cm^{-1} that are attributed to inorganic silicate matrix vibrations. More specifically, peaks are assigned as follows: 465s ρ(Si–O–Si), 800 m δ(Si–O–Si), 960w $\nu_{asym.}$(Si OH), 1080vs $\nu_{asym.}$(Si–O–Si) transverse-optical mode and 1223 m $\nu_{asym.}$(Si–O–Si) longitudinal-optical mode [45]. Spectrum (2a) displays also peaks owned to alkyl groups from the organic template that are defined as 1476w $\delta(CH_2)$, 2856s $\nu_{sym.}(CH_2)$ and 2924s $\nu_{asym.}(CH_2)$. Finally, additional peaks are ascribed to the naphthalene groups indicating the successful incorporation of the organosilicate precursor in the matrix of the sample. In particular, peaks by aryl groups are assigned as 780 m γ(CH), 3039w $\nu_{sym.}$(CH) and 3056w $\nu_{asym.}$(CH), while the peak at 780 cm^{-1}

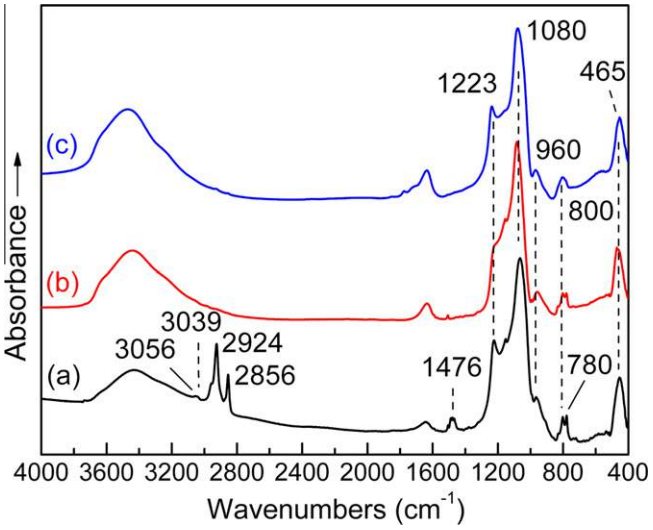

Fig. 2. FT infrared spectra of Naph-PNO (a), Naph-PNO-H^+ (b) and Naph-PNO-350 (c).

originates from the out-of-plane bending vibrations characteristic of naphthalene group [42,46].

Spectrum (2b) of sample Naph-PNO-H has the same silicate peaks with the pristine Naph-PNO, however, the peaks arising from the alkyl chains of the template are absent. The latest indicates the successful complete removal of the surfactant molecules by the ion-exchange reactions with HCl. Nevertheless, the characteristic peak of naphthalene at 780 cm^{-1} is still present which means that the ion-exchange reactions did not affect naphthalene groups suggesting that they were indeed incorporated in the matrix of the PNO during the co-condensation reaction. Spectrum (2c) of sample Naph-PNO-350 is similar to the spectrum (2b). In detail, there are only two minor differences between these two spectra. In fact, peak at 1223 cm^{-1} in spectrum (2c) is more distinct indicating a better ordering of uniform pores while naphthalene peak at 780 cm^{-1} is not clear enough although it is present as a shoulder in the silicate originated 800 cm^{-1} peak. These data are pointing out that both template removing techniques led to surfactant free samples while the attached naphthalene groups are intact.

The optical absorbance spectra of samples Naph-PNO (3a), Naph-PNO-H (3b) and Naph-PNO-350 (3c) are shown in Fig. 3, as calculated from diffuse reflectance experiments. All spectra in Fig. 3 show an almost similar broad convoluted absorption peak ranging from 200 to 325 nm, with slightly varied peak maximum position. Spectrum of the starting Naph-PNO and that of Naph-PNO-H^+ show also distinct well-defined narrow peaks at 317 nm and 313 nm, while the spectrum of the heat treated Naph-PNO-350 does not show these peaks. Moreover, all spectra exhibit an absorption peak or shoulder at ca. 230 nm, while the broad peak is centred at 296 nm in the spectrum of Fig. 3a and at 281 nm in the spectra of Fig. 3b and c. These absorption spectra resemble the spectrum of naphthalene, as also seen in the literature [47], where therein reported peaks in the 290 nm region appear in this work to be convoluted around the ~290 nm maximum, presumably due to the room temperature broadening as compared to Ref. [47]. In fact, the spectra in Fig. 3 have similar broadness and peak positions characteristics of naphthalene ethanol solution absorption spectrum, as for example reported by Pavia et al. [48]. It is important to note that naphthalene like active part, such as the one reported here, absorbs strongly at almost the naphthalene peak positions [49].

Moreover, the absorption peak of the sample in Fig. 3a appears to be red shifted compared to the other two samples. As reported later in the thermal measurements section, both H^+ and heat treated Naph-PNO samples have kept naphthalene content intact; however, optical absorption changes are detected. These are attributed to the increased interaction of the naphthalene molecule with the organic template, which is added to the silica matrix-naphthalene interaction, red shifting the optical spectra. The fact that no naphthalene–naphthalene dimer peaks are explicitly being observed is also evidence for the naphthalene–surfactant interaction. The naphthalene surfactant interaction has been observed before and shown that it is of this order of magnitude, as reported here, as for example in Ref. [50].

Photoluminescence emission (PL) and excitation (PLE) spectra of the prepared samples are shown in Fig. 4. Spectra of Naph-PNO are shown in 4a, 4b and 4c, with excitation at λ_{exc} = 250 nm, and monitoring at 400 nm and 450 nm, respectively. The excitation line at 250 nm allows for inclusion of all possible absorption mechanisms, but the 220 nm. It can be observed that the PL spectrum 4a is peaked at 384 nm, while the main responsible bands leading to this luminescence are detected from the PLE spectrum to be at 308 and 288 nm, in agreement with the absorbance spectrum. The PLE spectra 4b and 4c are exhibiting the structure of a multi-peaked absorption spectrum where all peaks at high energies have been convoluted. Naph-PNO sample's PL spectrum is red shifted with respect to the one reported by Stevens et al. of a naphthalene solution [51], possibly due to the position 1 modification of the naphthalene molecule or due to the interaction of the emitter with the silica matrix and the organic surfactant. Sample Naph-PNO-H^+ shows different luminescence properties, in accordance to decreased molecule interaction with

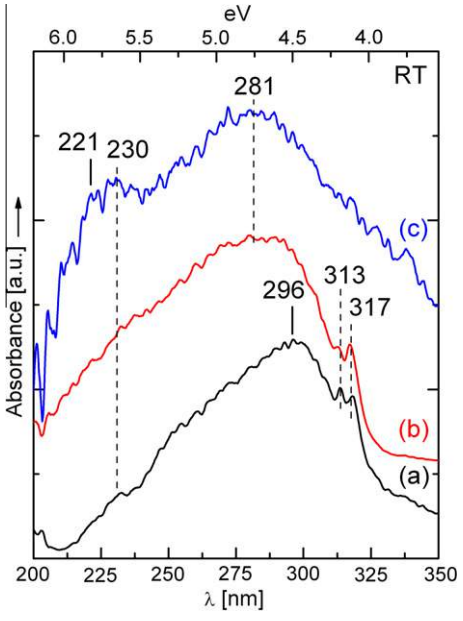

Fig. 3. Absorbance spectra of Naph-PNO (a), Naph-PNO-H^+ (b) and Naph-PNO-350 (c).

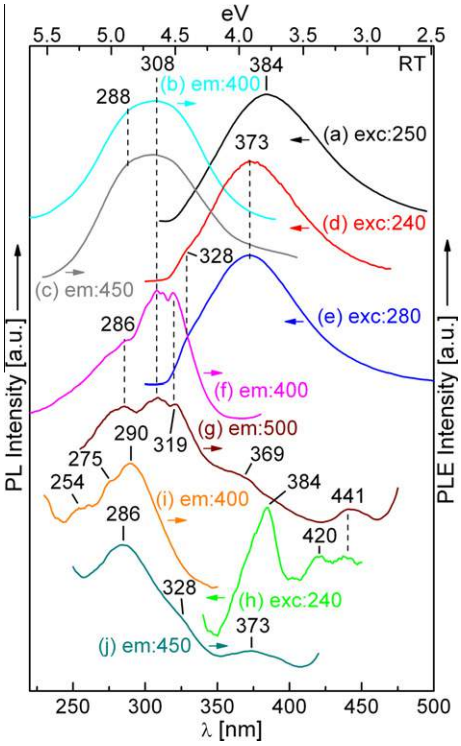

Fig. 4. PL (left) and PLE (right) spectra of samples Naph-PNO (a) excitation at 250 nm, (b) emission at 400 nm, (c) emission at 450 nm), Naph-PNO-H^+, (d) excitation at 240 nm, (e) excitation at 280 nm, (f) emission at 400 nm, g: emission at 500 nm) and Naph-PNO-350 (h) excitation at 240 nm, (i) emission at 400 nm and (j) emission at 450 nm).

the environment and, thus, slight blue shifting of the peaks observed in Fig. 4a–c. In particular, Fig. 4d–g shows the PL spectra observed with 240 nm and 280 nm excitation and the PLE spectra monitored at 400 and 500 nm, respectively. It can be observed that the PL spectra do show a broad peak centred at 373 nm, irrespectively of the excitation energy, while also exhibiting a small shoulder at 328 nm. On the other hand, the luminescence spectrum is mainly due to the absorption lines, as seen from the PLE spectra, at 319 nm, 308 nm and 286 nm, in agreement with the UV–vis spectra. Finally, it is also observed that PL at very low energies (*i.e.* 500 nm) is being also induced from absorption states at 369 and 441 nm showing the possibility of some, trivially luminescent states, which could be attributed to low energy excitons. Finally, the spectra of the heat treated sample, shown in Fig. 4h–j correspond to PL (λ_{exc} 240 nm) and PLE monitored at 400 and 450 nm, respectively. Despite the similarities of its absorption spectra with the other previously discussed samples, the heat treated sample shows decreased luminescence at low energies $\lambda > 420$ nm, but retains a small peak at 384 nm. The existence of this peak is attributed to naphthalene molecules, which were not further bridged to the silica matrix. Heat treatment does not decompose the emitter molecule as evidenced by the thermal analyses mentioned later on, but it is believed that the heat treatment forms more oxygen bridges with the silica matrix, thus, quenching the luminescence or by transferring energy to the silica matrix. Further evidence arises from XRD data, where the heat treatment shows that the pore structure has been constrained, thus, implying that the packing within the matrix has been altered. Moreover, the PLE spectra of the heat treated sample shows that the main absorption lines responsible for luminescence at low energies, ca. occur at the 286 and 328 nm. The PLE spectra are quite similar for the two different emission wavelengths, implying that the heat treatment has not altered significantly the naphthalene molecule which retains its original absorption mechanisms, but the luminescence is quenched. The latter could be attributed to the existence of triplet excitons due to the higher packing of the naphthalene moieties in the PNO network. Assuming that the absorption close to 312 nm line is due to the system I optical transitions (long axis) and the 280 nm is due to the system II optical transitions (small axis), it is rather evident that the heat treatment of the wall connected Naph-Si loses its symmetry along the long axis [47], which can occur if the end of the naphthalene molecule has bonded strongly with the silica matrix.

Overall evaluation of the optical absorption and luminescence results shows that the naphthalene like active part exhibits all the naphthalene absorption and luminescence bands, however, displaying small detuning due to the various interactions. These can be further controlled with the addition of other molecules to provide hybrid materials with energy transfer phenomena; even increased red shifted optical spectra.

Thermal DTA/TG/DTG diagrams of the Naph-PNO sample under oxygen flow are shown in Fig. 5. Sample is losing a ~3 wt.% up to 150 °C which can be attributed to moisture and physisorbed H_2O. From 150 °C to nearly 400 °C the sample is losing 31.4 wt.% as the template decomposes at 225 °C and is combusted at 337 °C with the relevant exothermic peak. Up to 500 °C the sample is losing another 4.7 wt.% attributed to some template residuals. From 500 °C to 650 °C the weight loss is 8.8 wt.% and a wide exothermic peak at 560 °C is also observed in the DTA signal. This loss is ascribed in the naphthalene groups while the width of the exothermic peak indicates that the stability of these groups varies, which can only be attributed to some relation of their exact position in the matrix and the number of the silicate oxygen bridges they share. Above 650 °C the sample is thermodynamically stable and the remained mass up to 1000 °C is slightly above 50 wt.% corresponding to the residual silica portion.

The analogous thermal DTA/TG/DTG diagrams of the Naph-PNO-H sample under oxygen flow are shown in Fig. 6. Sample is

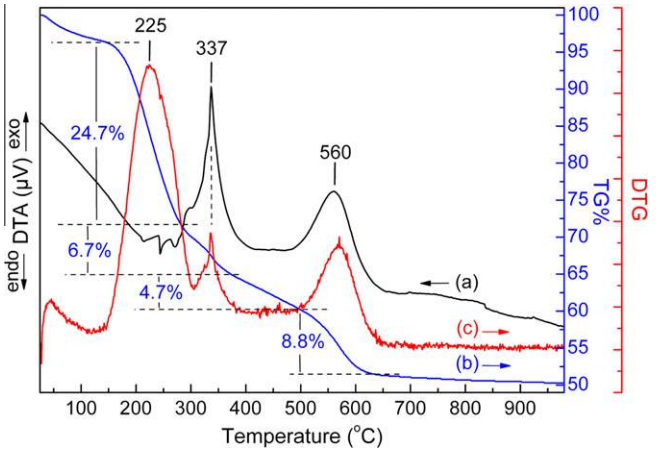

Fig. 5. DTA (a), TG (b) and DTG (c) diagrams of the Naph-PNO sample.

losing H_2O and residues up to 460 °C of about 13 wt.% without though showing any well defined peaks in the DTA signal. In the region 460–650 °C the sample is losing 14.9 wt.% with a corresponding exothermic peak at 550 °C assigned to the naphthalene groups, while it is also stable above 650 °C and remained mass up to 1000 °C is about 70 wt.%. The same thermal diagrams for the sample Naph-PNO-350 are shown in Fig. 7. Sample displays similar thermal behaviour and properties with Naph-PNO-H^+. Weight loss up to 350 °C is ~4 wt.%, from 350 °C to 700 °C sample loses 16.9 wt.% as naphthalene degrades with an observed exothermic peak at 535 °C and above 700 °C is stable with remained mass of about 77.5 wt.%. These results are discussed in detail later in the text.

Based on outcomes from previous works about the condensation of TEOS and organosilanes–as it is the Naph-Si in this work–for PNOs, the theoretical naphthalene molar concentration in the materials could approximately be calculated [18,30,52]. Specifically, if TEOS becomes fully condensed, Q^4 silica units are formed, were n in the Q^n groups [Q^n: $Si(OSi)_n(OH)_{4-n}$] stands for the number of oxygen bridges which each particular Si atom is sharing. For Naph-Si T^n units are created respectively, were n = 1–3. While Q^3 units are usually dominant from TEOS condensation followed by Q^4 units [18,52], for Naph-Si incomplete cross-linked T^2 and T^1 units should have higher concentration in comparison with the respective incomplete Q^2 and Q^1 groups in the case of TEOS because of the voluminous naphthalene group that hinders its

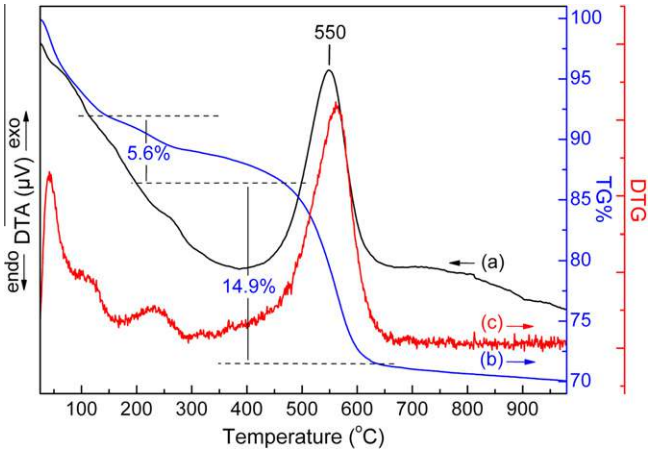

Fig. 6. DTA (a), TG (b) and DTG (c) diagrams of the Naph-PNO-H^+ sample.

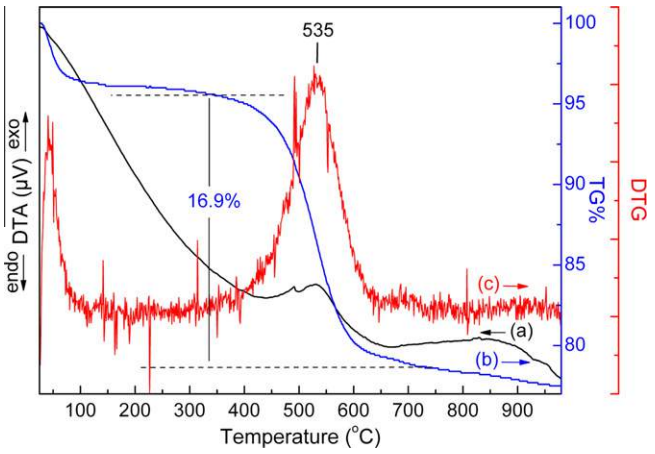

Fig. 7. DTA (a), TG (b) and DTG (c) diagrams of the Naph-PNO-350 sample.

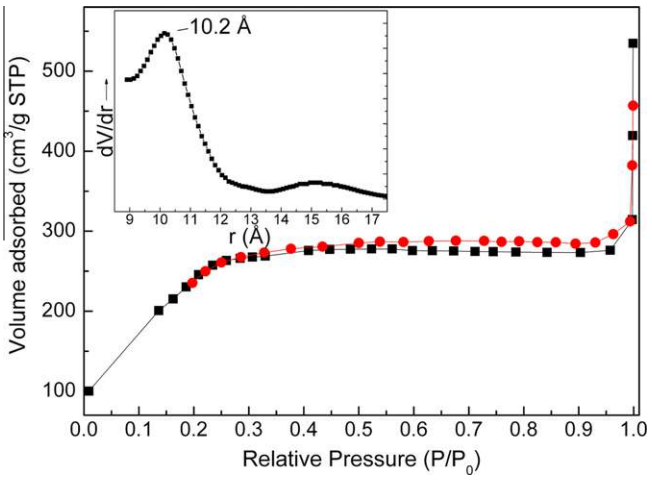

Fig. 8. Nitrogen adsorption–desorption isotherm of sample Naph-PNO-H. Inset: corresponding pore size distribution calculated with the Barrett–Joyner–Halenda method.

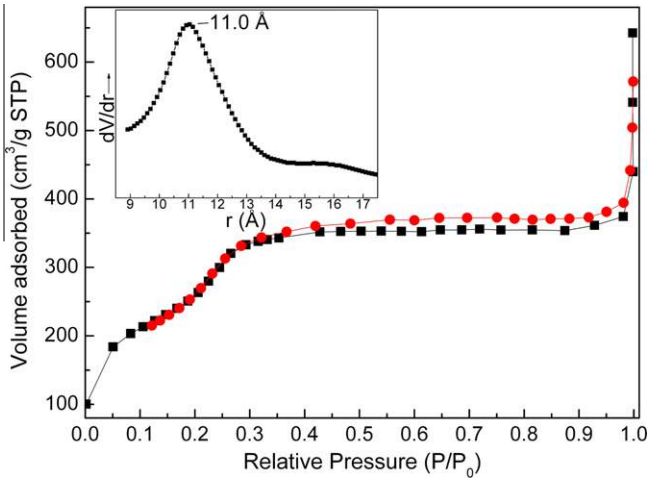

Fig. 9. Nitrogen adsorption–desorption isotherm of sample Naph-PNO-350. Inset: corresponding pore size distribution calculated with the Barrett–Joyner–Halenda method.

condensation [30]. Thus, for a rough theoretical calculation it has been assumed that TEOS should be condensed in such a way producing about 60% Q^3 and 40% Q^4 units, while Naph-Si should form mainly T^2 units (60%) and fewer percentages of T^1 (30%) and T^3 (10%) units. Hence, is concluded that theoretical maximum naphthalene weight quota for samples Naph-PNO-H^+ and Naph-PNO-350 is about 21.0% and molar concentration is 1.65 mmol/g. In fact, these values have limited bounds as upper (for higher condensed Q^n units and lesser condensed T^n units) and lower (for lesser condensed Q^n units and higher condensed T^n units) values, are close enough with the above assumed ones for weight percentage (±1%) and molar concentration (±0.08 mmol/g). Theoretical 21.0% can be compared with the relevant weight loss from the TG signals in Figs. 6 and 7. Although, sample Naph-PNO-H^+ seems to have a small template residue as naphthalene percentage is 14.9% and remained mass 70%. Therefore, values from sample Naph-PNO-350 are more logical and valid. The latter implies that practically the experimental naphthalene weight quota of both materials is ~16.9 wt.%. Compared to the theoretical 21.0% maximum content value, it is concluded that ~80% of the Naph-Si precursor was finally co-condensed to form the PNO. Additionally, the final naphthalene molar concentration is about 1.33 mmol/g.

The nitrogen adsorption desorption isotherms of samples Naph-PNO-H^+ and Naph-PNO-350 as well as their corresponding pore size distributions calculated with the BJH method (in the insets) are shown in Figs. 8 and 9. Both isotherms are categorized as type IV classification [53], which is characteristic of periodic nanoporous materials adsorption. The presence of a sharp sorption step in the adsorption curve of sample Naph-PNO-350, at P/P_0 of about 0.22, indicates that the sample possesses a well-defined array of regular nanopores. This sorption step is not as much distinct in the isotherm of sample Naph-PNO-H, however, there is a suspicion about an analogous possible small step at P/P_0 of about 0.20. In addition, based on the XRD pattern and especially on the fact that all three main reflection peaks appear in the patterns, it is supposed that the sample consists of uniform nanopores, yet naphthalene groups are attached in the matrix in a way to be located in the interior surface of the pores, influencing and changing that way the relative pressure that pores absorb nitrogen. This scenario is further explored in the pore size distribution discuss and analysis section.

Specific surface areas (S_{BET}) were calculated using BET equation and were found to be 1016 and 1076 m^2/g for samples Naph-PNO-H^+ and Naph-PNO-350 respectively [54,55]. Surface areas (S_t) were also determined from t-plots and were found 1174 and 1103 m^2/g, respectively [56]. In addition, macroporous and mesoporous surface areas (S_{macro} and S_{meso}, respectively) were calculated from t-plots. Sample Naph-PNO-H^+ appears not to have S_{macro} (~0) so S_{meso} is equal to 1174 m^2/g, while for sample Naph-PNO-350 S_{macro} = 36 m^2/g and S_{meso} = 1067 m^2/g. Pore volume (V_{pore}) at P/P_0 0.95 was 0.43 mL/g for Naph-PNO-H^+ and 0.57 mL/g for Naph-PNO-350. Microporous and mesoporous pore volume (V_μ and V_{meso}, respectively) were estimated at the same P/P_0 value (0.95). These were found V_μ: 0.08 mL/g and V_{meso}: 0.424 mL/g for Naph-PNO-H^+, and V_μ: ~0 and V_{meso}: 0.57 mL/g for Naph-PNO-350. Macroporous pore volume (V_{macro}) was estimated by the difference of V_{pore} between the P/P_0 values of 0.99 and 0.95. For sample Naph-PNO-H^+ V_{macro} was 0.049 mL/g, while for Naph-PNO-350 V_{macro} was 0.103 mL/g.

Besides surface area and pore volume, pore diameter of the samples was also estimated by various methods. Hydraulic pore diameter ($d_h = 4V_{pore}/S_{BET}$) was 16.9 Å for Naph-PNO-H^+ and 21.2 Å for Naph-PNO-350. Pore size distributions (PSD) of both samples (insets of Figs. 8 and 9) were created using Kelvin equation according to the Barrett–Joyner–Halenda (BJH) method and for sample Naph-PNO-H^+ the mean pore diameter was found d_{BJH}: 20.4 Å, while for Naph-PNO-350 d_{BJH}: 22.0 Å [57]. As pore diameters of the samples were in the microporous/mesoporous

Table 1
Pore parameters derived from X-ray diffraction patterns, nitrogen adsorption data and helium pycnometry. Specific surface area with Brunauer–Emmett–Teller method (S_{BET}), specific surface area from t-plot (S_t), pore volume at P/P_0 0.95 (V_{pore}), hydraulic pore diameter (d_h), mean pore diameter with Barrett–Joyner–Halenda method (d_{BJH}), mean pore diameter with Horvath–Kawazoe method (d_{H-K}), pore diameter with Kruk-–JaroniecSayari geometrical model (W_{KJS}), interplanar spacing (d_{100}), unit cell parameter (a_o), pore wall thickness (π), pore wall skeletal density (d_{skelet}).

Sample	S_{BET} (m^2/g)	S_t (m^2/g)	V_{pore} (mL/g)	d_h (Å)	d_{BJH} (Å)	d_{H-K} (Å)	W_{KJS} (Å)	d_{100} (Å)	a_o (Å)	π (Å)	d_{skelet} (g/mL)
Naph-PNO-H^+	1016	1174	0.43	16.9	20.4	21.6	35.3	42.4	48.9	28.5	2.068
Naph-PNO-350	1076	1103	0.57	21.2	22.0	25.0	33.6	38.1	44.0	22.0	1.96

boundary, PSD calculations were also performed using the Lennard-Jones potential functions according to the Horvath–Kawazoe method which is better for microporous materials [58,59], from which the mean pore diameter of both samples was calculated and found 21.6 Å for Naph-PNO-H^+ and 25.0 Å for Naph-PNO-350. In fact, the shape of the PSD curves from the H–K method (Figs. S3 and S4 available as Supplementary material) agrees with the hypothesis mentioned previously about the influence of the naphthalene groups in the adsorption relative pressure as in the PSD curve of sample Naph-PNO-H^+ the mean pore diameter is not as dominant as in the case of Naph-PNO-350 leading in a lack of a sharp sorption step in adsorption curve of its' relative nitrogen adsorption isotherm. However, taking into account the DTA analysis, another possible scenario may be adopted; the small amount of remaining surfactant in the Naph-PNO-H^+ sample could lead to an apparent smaller pore size compared with Naph-PNO-350, along with wider pore size distribution and reduced pore volume of this sample.

The Kruk–Jaroniec–Sayari (KJS) geometrical model was also used for the pore diameter calculation [60,61], though this model slightly overestimates the diameter while BJH tends to underestimate it [62]. The KJS geometrical model is based in the following formula:

$$W_{KJS} = cd_{100}[d_{skelet}\nu_{pore}/(1 + d_{skelet}\nu_{pore})]^{1/2} \quad (1)$$

where W_{KJS} is the pore diameter, $c = [8/(3^{1/2}\pi)]^{1/2} = 1.213$ is a constant, d_{100} is the (100) interplanar spacing, d_{skelet} is the skeletal density of pore walls of the samples (measured by helium pycnometry as mentioned later) and V_{pore} is the pore volume, equal to 0.43 mL/g and 0.57 mL/g for Naph-PNO-H^+ and Naph-PNO-350 samples, respectively as estimated from the nitrogen adsorption–desorption isotherms (Table 1). Using formula (2) pore diameter W_{KJS} of Naph-PNO-H^+ was calculated at 35.3 Å and for Naph-PNO-350 was 33.6 Å. These calculated values differ from the determined by the BJH and H–K methods (that are in good agreement) as it is a fact that the KJS model overestimates the pore diameter. In general, all the above data from nitrogen porosimetry suggest that both samples possess nanopores in the microporous/mesoporous borderline with high specific surface areas.

Skeletal densities of the samples were calculated by helium pycnometry at room temperature and atmospheric pressure that resulted for sample Naph-PNO-H^+ a d_{skelet} of 2.068 g/mL. For sample Naph-PNO-350 measured value was 1.96 g/mL. Besides their employment in estimating various useful data about the materials, skeletal densities also confirm naphthalene's incorporation in the PNO matrix as these values are quite lower than the density of amorphous silica (2.2 g/mL) that is regularly used as reference for analogous silicate materials [21]. Finally, apparent densities of both samples were calculated by setting the appropriate quantity of the powders in a container of known volume, without pressing the powders, and by dividing the measured weight of the powders with this volume. The above procedure resulted a d_{appar} of ~0.13 g/mL for both samples. The most significant pore parameters derived from X-ray diffraction patterns, nitrogen adsorption data and helium pycnometry for the two samples are summarized in Table 1. Combining data from these techniques it can be calculated and concluded that even though the pore diameter of both samples is about the same, the silica matrix width in the heat treated sample is significantly smaller (22.0 compared to 28.5 Å), as a result from the formation of more oxygen bridges, which agrees with the optical observations about quenched luminescence in this sample. Moreover, comparing the wall thickness (π) of the non-calcined sample Naph-PNO-H^+ (28.5 Å) with non-calcined pure silica mesoporous materials like MCM-41, it is observed that non-calcined MCM-41 samples prepared with the same synthetic route do have thinner π at about 18–22 Å [21,44,45]. This difference probably originates from the incorporation of the voluminous naphthalene silane groups in the walls.

4. Conclusions

In the present work we report the synthesis and the structural characterization of novel naphthalene containing periodic nanoporous organosilicates. Final materials exhibit ultimate properties for application in the field of hydrogen and methane storage, as they comprise high naphthalene content up to 17 wt.% with a corresponding 1.33 mmol/g naphthalene molar concentration as confirmed by the %TG signals, high crystallinity as evidenced by the X-ray diffraction patterns, specific surface area above 1000 m^2/g and pore size distributions in the microporous/mesoporous boundary as estimated by nitrogen porosimetry. Materials also display skeletal density of ~2 g/mL as calculated by helium pycnometry. Moreover, the simple one end attachment of the absorptive and luminescent naphthalene like molecules demonstrates the application of these materials in optical and possible optoelectronic applications. Concerning both sorption and optical applications, possible enhancement routes of the reported work include: (a) the alteration of the naphthalene molecule with other polyaromatic molecules, (b) the encompassing of different functional groups at the 6 or 7 positions of naphthalene, (c) the combination of various organic luminescent molecules and (d) the inclusion of molecules with higher optical nonlinearity.

Acknowledgments

The authors would like to acknowledge the use of the XRD unit and the NMR Centre of the Laboratory Network of the University of Ioannina for measurements.

Appendix A. Supplementary data

Supplementary data associated with this article can be found, in the online version, at http://dx.doi.org/10.1016/j.micromeso.2012.03.037.

References

[1] C.T. Kresge, M.E. Leonowicz, W.J. Roth, J.C. Vartuli, J.S. Beck, Nature 359 (1992) 710.
[2] J.S. Beck, J.C. Vartuli, W.J. Roth, M.E. Leonowicz, C.T. Kresge, K.D. Schmitt, J. Am. Chem. Soc. 114 (1992) 10834.

[3] D. Zhao, J. Feng, Q. Huo, N. Melosh, G.H. Frederickson, B.F. Chmelka, G.D. Stucky, Science 279 (1998) 548.
[4] D. Zhao, Q. Huo, J. Feng, B.F. Chmelka, G.D. Stucky, J. Am. Chem. Soc. 120 (1998) 6024.
[5] S.A. Bagshaw, E. Prouzet, T.J. Pinnavaia, Science 269 (1995) 1242.
[6] C. Yu, Y. Yu, D. Zhao, Chem. Commun. (2000) 575.
[7] Y. Meng, D. Gu, F. Zhang, Y. Shi, L. Cheng, D. Feng, Z. Wu, Z. Chen, Y. Wan, A. Stein, D. Zhao, Chem. Mater. 18 (2006) 4447.
[8] R. Ryoo, J.M. Kim, C.H. Ko, C.H. Shin, J. Phys. Chem. 100 (1996) 17718.
[9] R. Ryoo, S.H. Joo, S. Jun, J. Phys. Chem. B 103 (1999) 7743.
[10] S. Jun, S.H. Joo, R. Ryoo, M. Kruk, M. Jaroniec, Z. Liu, T. Ohsuna, O. Terasaki, J. Am. Chem. Soc. 122 (2000) 10712.
[11] S. Inagaki, S. Guan, Y. Fukushima, T. Ohsuna, O. Terasaki, J. Am. Chem. Soc. 121 (1999) 9611.
[12] B.J. Melde, B.T. Holland, C.F. Blanford, A. Stein, Chem. Mater. 11 (1999) 3302.
[13] T. Asefa, M.J. MacLachlan, N. Coombs, G.A. Ozin, Nature 402 (1999) 867.
[14] F. Hoffmann, M. Cornelius, J. Morell, M. Fröba, Angew. Chem. Int. Ed. 45 (2006) 3216.
[15] M.C. Burleigh, M.A. Markowitz, M.S. Spector, B.P. Gaber, J. Phys. Chem. B 105 (2001) 9935.
[16] C.P. Jaroniec, M. Kruk, M. Jaroniec, A. Sayari, J. Phys. Chem. B 102 (1998) 5503.
[17] S. Parambadath, V.K. Rana, S. Moorthy, S.-W. Chu, S.-K. Park, D. Lee, G. Sung, C.-S. Ha, J. Solid State Chem. 184 (2011) 1208.
[18] S. Parambadath, V.K. Rana, D. Zhao, C.-S. Ha, Micropor. Mesopor. Mater. 141 (2011) 94.
[19] W. Na, Q. Wei, J.-N. Lan, Z.-R. Nie, H. Sun, Q.-Y. Li, Micropor. Mesopor. Mater. 134 (2010) 72.
[20] K.F. Lam, K.L. Yeung, G. McKay, Langmuir 22 (2006) 9632.
[21] K. Dimos, P. Stathi, M.A. Karakassides, Y. Deligiannakis, Micropor. Mesopor. Mater. 126 (2009) 65.
[22] F. Hoffmann, M. Fröba, Chem. Soc. Rev. 40 (2011) 608.
[23] N. Mizoshita, T. Tani, S. Inagaki, Chem. Soc. Rev. 40 (2011) 789.
[24] V. Rebbin, R. Schmidt, M. Fröba, Angew. Chem. Int. Ed. 45 (2006) 5210.
[25] Q. Yang, J. Liu, L. Zhang, C. Li, J. Mater. Chem. 19 (2009) 1945.
[26] N. Yu, Y. Ding, A.-Y. Lo, S.-J. Huang, P.-H. Wu, C. Liu, D. Yin, Z. Fu, D. Yin, C.-T. Hung, Z. Lei, S.-B. Liu, Micropor. Mesopor. Mater. 143 (2011) 426.
[27] S.A. Trammell, B.J. Melde, D. Zabetakis, J.R. Deschamps, M.A. Dinderman, B.J. Johnson, A.W. Kusterbeck, Sens. Actuators, B 155 (2011) 737.
[28] P. Stathi, K. Dimos, M.A. Karakassides, Y. Deligiannakis, J. Colloid Interface Sci. 343 (2010) 374.
[29] W. Wang, J.E. Lofgreen, G.A. Ozin, Small 6 (2010) 2634.
[30] N. Mizoshita, Y. Goto, M.P. Kapoor, T. Shimada, T. Tani, S. Inagaki, Chem. Eur. J. 15 (2009) 219.
[31] T. Tani, N. Mizoshita, S. Inagaki, J. Mater. Chem. 19 (2009) 4451.
[32] S. Inagaki, O. Ohtani, Y. Goto, K. Okamoto, M. Ikai, Angew. Chem. Int. Ed. 48 (2009) 4042.
[33] T. Okada, Phys. Chem. Chem. Phys. 13 (2011) 7961.
[34] Y. Goto, K. Nakajima, N. Mizoshita, M. Suda, N. Tanaka, T. Hasegawa, T. Shimada, T. Tani, S. Inagaki, Micropor. Mesopor. Mater. 117 (2009) 535.
[35] X. Guo, H. Guo, L. Fu, H. Zhang, R. Deng, L. Sun, J. Feng, S. Dang, Micropor. Mesopor. Mater. 119 (2009) 252.
[36] S.M. Seo, E.J. Cho, S.J. Lee, K.C. Nam, S.-H. Park, J.H. Jung, Micropor. Mesopor. Mater. 114 (2008) 448.
[37] J.H. Jung, W.S. Han, J.A. Rim, S.J. Lee, S.J. Cho, S.Y. Kim, J.K. Kang, S. Shinkai, Chem. Lett. 35 (2006) 32.
[38] U. Martinez, G. Pacchioni, Micropor. Mesopor. Mater. 129 (2010) 62.
[39] M. Kubo, K. Ishiyama, A. Shimojima, T. Okubo, Micropor. Mesopor. Mater. 147 (2012) 194.
[40] M.K. Antoniou, A. Policicchio, K. Dimos, D. Gournis, M.A. Karakassides, R.G. Agostino, Micropor. Mesopor. Mater. (2012), http://dx.doi.org/10.1016/j.micromeso.2012.03.035.
[41] A.S.-Y. Lee, Y.-T. Chang, S.-F. Chu, K.-W. Tsao, Tetrahedron Lett. 47 (2006) 7085.
[42] Z.Y. Tang, Y. Zhang, T. Wang, W. Wang, Synlett 2010 (2010) 804.
[43] B. Panella, M. Hirscher, S. Roth, Carbon 43 (2005) 2209.
[44] K. Dimos, I.B. Koutselas, M.A. Karakassides, J. Phys. Chem. B 110 (2006) 22339.
[45] K. Dimos, Ľ. Jankovič, I.B. Koutselas, M.A. Karakassides, R. Zbořil, P. Komadel, J. Phys. Chem. C 116 (2012) 1185.
[46] S.A. Sandford, M.P. Bernstein, L.J. Allamandola, Astrophys. J. 607 (2004) 346.
[47] A. Bree, T. Thirunamachandran, Mol. Phys. 5 (1962) 397.
[48] D.L. Pavia, G.M. Lampman, G.S. Kriz, J.R. Vyvyan, Introduction to Spectroscopy, fourth ed., Brooks/Cole, Cengage Learning, Belmont, USA, 2009.
[49] K. Hirayama, Handbook of Ultraviolet and Visible Absorption of Organic Compounds, Plenum Press Data Division, New York, USA, 1967.
[50] K. Mathauer, C.W. Frank, Langmuir 9 (1993) 3002.
[51] B. Stevens, Spectrochim. Acta 18 (1962) 439.
[52] X.S. Zhao, G.Q. Lu, A.K. Whittaker, G.J. Millar, H.Y. Zhu, J. Phys. Chem. B 101 (1997) 6525.
[53] K.S.W. Sing, D.H. Everett, R.A.W. Haul, L. Moscou, R.A. Pierotti, J. Rouquerol, T. Siemieniewska, Pure Appl. Chem. 57 (1985) 603.
[54] S. Brunauer, P.H. Emmett, E. Teller, J. Am. Chem. Soc. 60 (1938) 309.
[55] M.R. Bhambhani, P.A. Cutting, K.S.W. Sing, D.H. Turk, J. Colloid Interface Sci. 38 (1972) 109.
[56] B.C. Lippens, J.H. De Boer, J. Catal. 4 (1965) 319.
[57] E.P. Barrett, L.G. Joyner, P.P. Halenda, J. Am. Chem. Soc. 73 (1951) 373.
[58] G. Horvath, K. Kawazoe, J. Chem. Eng. Jpn. 16 (1983) 470.
[59] L.S. Cheng, R.T. Yang, Chem. Eng. Sci. 49 (1994) 2599.
[60] M. Kruk, M. Jaroniec, A. Sayari, J. Phys. Chem. B 101 (1997) 583.
[61] M. Kruk, M. Jaroniec, A. Sayari, Micropor. Mesopor. Mater. 27 (1999) 217.
[62] W. Zhang, C.I. Ratcliffe, I.L. Moudrakovski, J.S. Tse, C.-Y. Mou, J.A. Ripmeester, Micropor. Mesopor. Mater. 79 (2005) 195.